Materials & Design 231 (2023) 112041

Contents lists available at ScienceDirect

Materials & Design

journal homepage: www.elsevier.com/locate/matdes

Discontinuous dynamic recrystallization and nucleation mechanisms associated with 2-, 3- and 4-grain junctions of polycrystalline nickel-based superalloys

Bingchao Xie [a], Heng Li [a], Yongquan Ning [a,*], Mingwang Fu [b]

[a] School of Materials Science and Engineering, Northwestern Polytechnical University, Xi'an 710072, PR China
[b] Department of Mechanical Engineering, The Hong Kong Polytechnic University, Kowloon, Hong Kong, China

HIGHLIGHTS

- Dynamic recrystallization grains nucleated at 4-, 3- and 2-grain junctions in turn.
- Two proposed recrystallization nucleation mechanisms operate well at grain junctions.
- The nucleation priority of one grain junction can be predicted by Taylor factors.

GRAPHICAL ABSTRACT

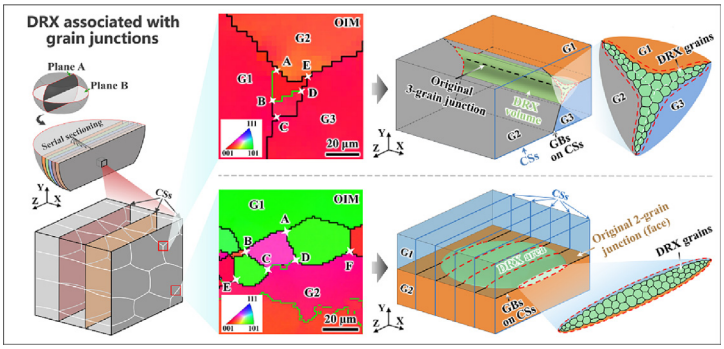

ARTICLE INFO

Article history:
Received 12 February 2023
Revised 10 May 2023
Accepted 24 May 2023
Available online 30 May 2023

Keywords:
Grain junctions
Nucleation priority
Nucleation mechanism
4-grain stacking structure
Microstructure evolution
Nickel-based superalloys

ABSTRACT

Despite the important role of grain junctions to the dynamic recrystallization (DRX) of nickel-based superalloys, the nucleation mechanisms operating there and the influence factors besides deformation condition on nucleation priority are still unclear. The microstructure evolution considering grain junction effects has not been explored in depth yet. In this paper, DRX nucleation at the 2-, 3- and 4-grain junctions of a nickel-based superalloy was investigated. A proposed passive grain boundary bulging (PGBB) mechanism operated well at 2-grain junctions, and accounted for the continuity of necklace structure during the early stage of hot deformation. For the 3-grain junctions, a two-step strain-induced bulging of grain boundary fragments, which closely adjoined the junctions, was found to dominate the DRX nucleation. In addition, an increasing nucleation priority from 2-, 3- to 4-grain junctions was confirmed by the established thermodynamic model, while the nucleation priority differences of the same kind grain junctions were quantitatively analyzed by using the Taylor factors of their component grains. Finally, the DRX microstructure evolution of a 4-grain stacking unit during hot deformation was described. The understanding of DRX associated with 2-, 3- to 4-grain junctions made it more effective to tailor the microstructure of nickel-based superalloy forgings.

1. Introduction

Nickel-based superalloys are widely used in the manufacture of aero-engine turbine disks due to their excellent mechanical properties at high temperature, and hot deformation is still the main

* Corresponding author.
E-mail address: luckyning@nwpu.edu.cn (Y. Ning).

https://doi.org/10.1016/j.matdes.2023.112041
0264-1275/

manufacturing process for the disks despite the rapid development of powder metallurgy and 3D printing technologies [1-5]. Dynamic recrystallization (DRX) is the core element during the hot deformation process of nickel-based superalloys, which strongly affects the microstructure and hence the mechanical properties of the disk forgings [6,7]. Numerous investigations have been conducted to understand the DRX behaviors and nucleation mechanisms of nickel-based superalloys [8,9]. Due to the low stacking fault energy (SFE) of nickel-based superalloys, DRX nuclei usually prefer to form first at junctions consisting of two or more grains, rather than in grain interiors or other potential nucleation sites during hot deformation [10,11]. This type of DRX is termed discontinuous DRX by a phenomenological classification criterion in consideration of its clear nucleation and growth stages [12]. Preexisting studies have confirmed that the grain boundary (GB) bulging mechanism usually operates well during the discontinuous DRX nucleation process in low SFE alloys, provided that only the random grain boundaries (GBs) are taken into account in the 2D case [13,14]. However, polycrystalline metallic materials, with a cellular structure, consist of grains and different grain junctions, including faces, edges and vertices, in the actual 3D case. According to the conservation law of Euler's equation, there are no more than four grains joining the same vertex for the face-centered cubic model arranged by Kelvin tetrakaidecahedron [15]. Similarly, the numbers of grains joining a given edge or face can be determined to be three or two, respectively. Therefore, the grain junctions, i.e., faces, edges and vertices, of nickel-based superalloys are referred to as 2-, 3- and 4-grain junctions for visualization in the following text.

The geometric and crystallographic properties of grain junctions strongly influence the behaviors, thermodynamics and kinetics of nucleation, which has been verified both in DRX and solid-state phase transformation cases in part, although the related works are limited. Hence, it deserves special attention to explore the DRX nucleation at 2-, 3- and 4-grain junctions to understand the microstructure evolution during hot deformation of polycrystalline nickel-based superalloys. Most available studies on DRX nucleation to date are focused on 2-grain junctions, i.e., GBs, due to their large amounts as well as the nucleation priority exhibiting there [14,16,17]. GB motion, including bulging, sliding and shearing, has been found to dominate the DRX nucleation at 2-grain junctions [18-20]. The factors that affect GB motion and consequently the DRX nucleation are also being studied recently [21,22]. It should be noted that the investigations mentioned above are all focused on the nucleation process of the first DRX grains at original GBs, and the strain-induced grain boundary bulging (SIGBB) is thought to be the mainly nucleation mechanism for these DRX grains. While this mechanism operates well during the first DRX grains' nucleation, the formation of the continuous necklace structure, instead of an interrupted one, during the early stage of DRX cannot be explained. In addition, the nucleation after new grains engulfing the original 2-grain junctions should also be concerned, which matter much to the DRX microstructure evolution from GB regions to the interiors of deformed grains.

The 3-grain junctions are also essential components of polycrystalline alloys, since their number is comparable in the order of magnitude with that of 2-grain junctions [23]. Therefore, 3-grain junctions deserve special attention when one tries to understand the DRX process in nickel-based superalloys. The limited available reports about DRX at 3-grain junctions were all restricted to copper and stainless steel. Research on a copper tricrystal found that DRX grains nucleated at the 3-grain junctions at a strain much lower than the peak strain, which was attributed to the stress and strain concentrations induced by folding and GB sliding at 3-grain junctions [24,25]. Meanwhile, the twinning process was confirmed to accelerate DRX nucleation there. Subsequent studies on polycrystalline copper and Fe-32 %Ni stainless steel obtained more precise statistical results, which demonstrated the foregoing conclusions about DRX at 3-grain junctions [26,27]. However, the essential mechanism of twinning nucleation operating at 3-grain junctions was still unclear, since the above conclusion about twinning nucleation was based on the observation that most grains nucleating at 3-grain junctions were twins. In addition, the DRX nucleation priority of each individual 3-grain junction was affected by the character of the component GBs of the junctions, while only the 3-grain junctions which included twin boundaries were the focuses of previous studies [28]. Therefore, the 3-grain junctions consisting of random GBs, which are more common and the majority, must be focused, especially on the nucleation priority and the corresponding influencing factors. There is scarcely any available report for the DRX at 4-grain junctions, although these junctions are reasonably expected to be important sites for deformation inhomogeneities, and hence strongly influence DRX nucleation and subsequently microstructure evolution, as well as finally the mechanical properties [29]. This may be attributed to the complexities of microstructure characterization and theoretical analysis for 4-grain junctions.

In summary, the investigations on DRX at grain junctions of nickel-based superalloys were limited, particularly on the nucleation priority of each individual junction and the nucleation mechanisms operating here. In the present study, attention was hence focused on DRX nucleation at the 2-, 3- and 4-grain junctions of superalloy. DRX nucleation mechanisms operated at these junctions were confirmed first, and then their nucleation priorities were evaluated both by microstructure characterization and a proposed thermodynamic model, which was followed by quantitative analyses of the dependence of DRX nucleation on the crystal orientation of junctions' component grains. These works, with the 3D microstructure observation of grain junctions in addition, finally realized the exploration of the microstructure evolution of the 4-grain stacking unit during hot deformation, which helped to accurately tailor microstructure for the special mechanical property requirements of turbine disk forgings.

2. Materials and experiments

Cylindrical samples for uniaxial compression tests were machined from the columnar grain zone of a homogenized GH4720Li superalloy ingot with the chemical composition (wt.%) shown in Table 1. This superalloy was hardened by γ' precipitates, and the γ' solvus temperature was estimated to be 1160 °C. The whole ingot was annealed at 1180 °C for 4 h to eliminate the γ'+γ eutectic phase and prime γ' phase precipitating during the casting process to obtain a better deformation capability, which also produced a large initial grain size as expected (a mean major axis diameter of 1321.0 μm and a mean minor axis diameter of 201.3 μm, Fig. 1). The large initial columnar grains made it easy to identify the DRX grains to avoid any confusion.

All the samples, with a diameter and a height of 8 mm and 12 mm, for hot deformation were prepared to have their loading direction perpendicular to the columnar grain growth direction (Fig. 1(a)). Compression tests were conducted using a Gleeble-3500 simulator at 1140 °C with a strain rate of 0.1 s^{-1}. Tantalum foils with a thickness of 0.1 mm were placed between samples and dies to minimize friction and avoid adhesion. The samples were heated up to 1140 °C at a heating rate of 10 °C/s, and then held for 5 min to ensure temperature equilibrium. Hot deformation were interrupted at strains of 0.13 and 0.69, and were followed by water quenching immediately.

The deformed samples were sectioned parallel to the loading direction through the centerline, and the characterization sections (CSs) for observation of 3- and 2-grain junctions were ensured to

Table 1
Chemical composition of the superalloy used in this work (wt.%).

Cr	Co	Mo	Al	Ti	B	C	W	Ni
16.00	14.95	3.00	2.50	5.00	0.015	0.015	1.50	Bal.

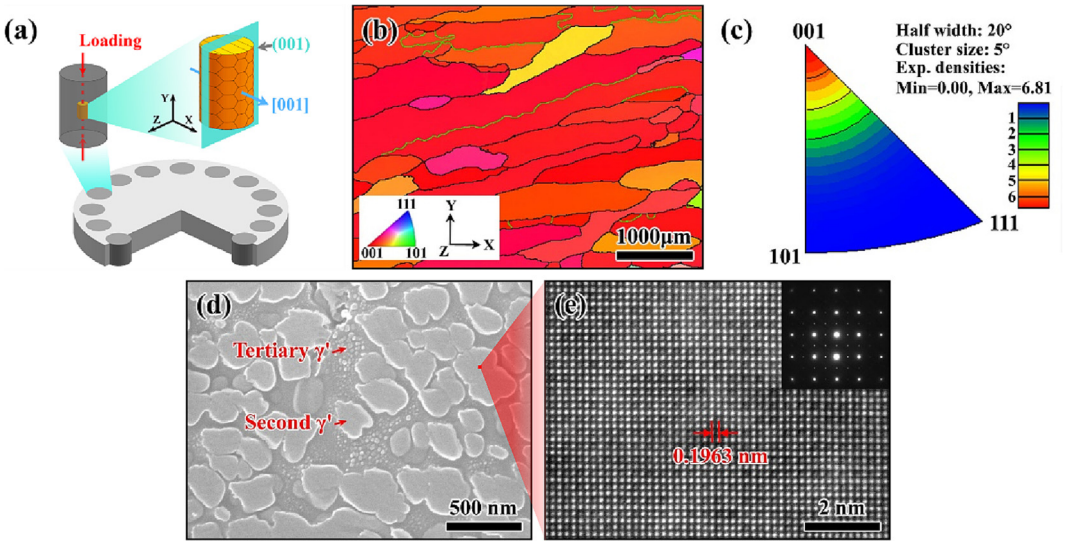

Fig. 1. Overview of the experimental material: (a) sampling position for hot deformation experiments; (b) orientation imaging microscopy (OIM) image along X direction obtained on the transverse plane of the deformation samples; (c) the corresponding inverse pole figure (IPF) along the X direction in (b); (d) the γ' phase captured by FEGSEM; (e) HRTEM images recorded at the second γ' phase.

be perpendicular (type A) and parallel (type B) to the columnar grain growth direction, respectively. The geometric features of columnar grains could hence be fully utilized to capture the DRX nucleation processes at corresponding grain junctions, which eliminated the sectioning effects of random characterization sections. Scanning electron microscopy (SEM), electron backscatter diffraction (EBSD), transmission electron microscopy (TEM) and high resolution transmission electron microscopy (HRTEM) were employed to characterize the microstructure in this work. All the CSs were mechanically ground first and then processed in accordance with the requirements of the different characterization techniques above. The samples for SEM observation were etched chemically using a solution of 100 ml HCl + 100 ml C_2H_5OH + 10 g $CuCl_2$, and then a Tescan MIRA3 XM field emission gun scanning electron microscopy (FEGSEM) was employed. EBSD tests were also carried out by the FEGSEM after the CSs were mechanically ground and then polished using a Buehler VibroMet 2 polisher. The scanning step size ranged from 1 to 3 μm according to demand, and relevant data analyses were conducted by using Oxford Instruments' HKL Channel 5 software.

3D observations were carried out through layer-by-layer polishing on a series of CSs to study the microstructure evolution within the 4-grain stacking unit during hot deformation. The samples for 3D observations were cut along planes A and B, and one of the four blocks was used for subsequent tests (Fig. 2). Planes A and B, as well as a series of planes parallel to the former, would be the CSs for microstructure characterization. Mechanical grinding processes with the same down force and the same time generated a uniform spacing between the CSs, which helped to study the DRX microstructure evolution within a 4-grain stacking unit. The CSs, of course, must be polished after each mechanical grinding process and then chemically etched using the solution mentioned above before microstructure characterization.

3. Results and discussion

3.1. Preferential DRX nucleation and mechanisms at grain junctions

3.1.1. Preferential nucleation at grain junctions

Fig. 3 shows the microstructures of GH4720Li type A samples that were deformed to a strain of 0.13 at 1140 °C with a strain rate of 0.1 s^{-1}. The area fraction of DRX grains was 1.6%, and almost all fine grains were located at the 2- and 3-grain junctions instead of the deformed grains' interiors, which was attributed to the dislocation pileup near the grain junctions (Fig. 3(b) and (c)). Specifically, 61.6% of the DRX grains mentioned above formed at 3-grain junctions, while the other 38.4% of them formed at 2-grain junctions. The mean equivalent diameter of the former was 18.6 μm, and the latter was 17.0 μm. In addition, only 25.0% of the original 2-grain junctions activated the DRX nucleation mechanism and formed at least one DRX grain, whereas 77.4% of the 3-grain junctions were engulfed by DRX grains. The statistical data above, which were obtained from several microstructure images under the same deformation conditions, indicate that 3-grain junctions are definitely preferential nucleation sites for DRX compared to 2-grain junctions. DRX nucleation thermodynamic investigation of grain junctions would help to explain this, but the DRX nucleation process and corresponding nucleation mechanisms at the two typical nucleation sites must be studied first.

3.1.2. Nucleation mechanisms at 2-grain junctions

Type B samples help to capture the DRX process at 2-grain junctions under a lower strain condition, especially the nucleation process. As shown in Fig. 4(a), grains G1 and G2 were identified to be deformed grains based on the kernel average misorientation (KAM) distribution and microstructure morphology, while these fine

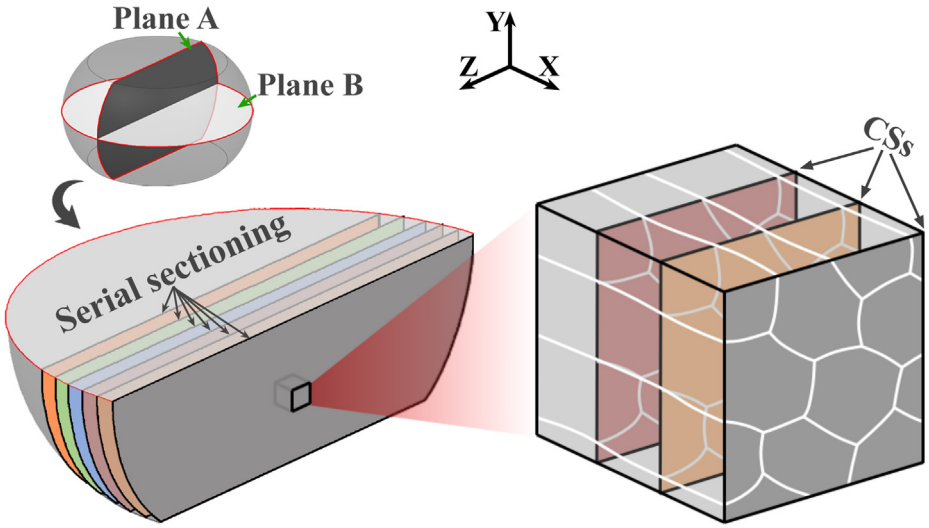

Fig. 2. Schematic of 3D observation through the microstructure characterization of serial CSs.

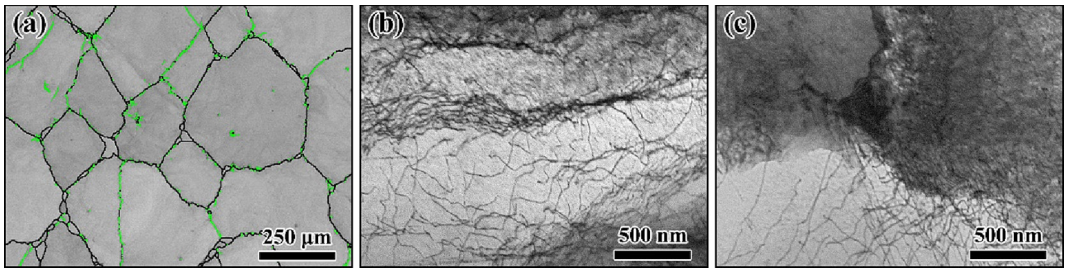

Fig. 3. Microstructure of GH4720Li type A samples deformed at 1140 °C with a strain rate of 0.1 s^{-1}: (a) band contrast image obtained by EBSD; (b)-(c) dislocation pileup near the original 2- and 3-grain junctions, respectively.

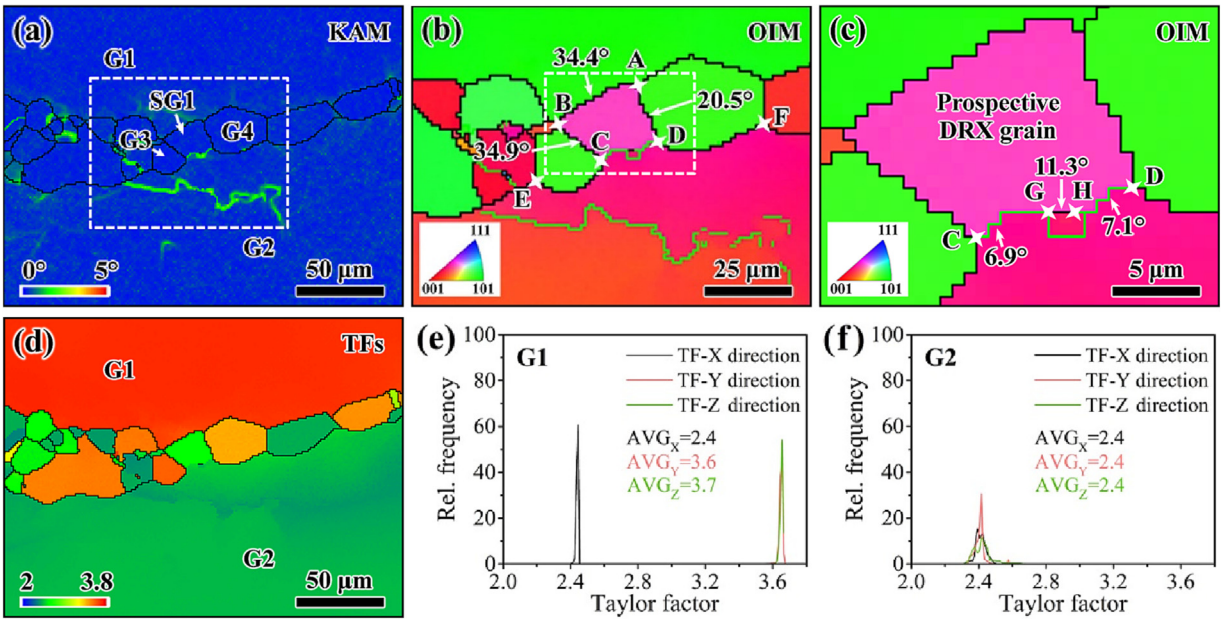

Fig. 4. Microstructure at the 2-grain junctions of type B samples compressed to a strain of 0.13 at 1140 °C with a strain rate of 0.1 s^{-1}: (a) KAM map; (b) OIM image along Z direction; (c) selected magnification of (b); (d)-(f) Taylor factor distribution (CD, {1 1 1} ⟨1 1 0⟩).

grains/subgrains between G1 and G2 were DRX grains or prospective DRX grains. The latter referred to the special subgrains that were closed by the original GBs and the newborn subgrain boundaries together. Obvious GB bulging towards the high KAM area indicated that the nucleation through strain-induced GB migration dominated the DRX processes at the 2-grain junctions, which was

identified as a discontinuous DRX in the phenomenological categorization [14,30]. Two different micromechanisms associated with GB bulging were found to control the nucleation processes here. Obvious GB bulging towards G2 could be observed when one focused on DRX grain G3. This bulging GB separated the strain-free volume from deformed grain G2 and continued migrating towards G2 driven by the dislocation density difference. It is a classical DRX nucleation mechanism based on SIGBB, and has been verified during the hot deformation process of several nickel-based superalloys [30,31]. The thing that matters is although the SIGBB mechanism operates well during the nucleation process of G3, it is not suitable for the nucleation of the adjacent prospective DRX grain, i.e., the subgrain SG1 here.

As shown in Fig. 4(b) and (c), SG1 was separated from other grains by several GB fragments, which were significantly distinct in profile features from those closing G3. The GB fragment A-B was almost straight but still closed a strain-free volume with fragments B-C, C-D and A-D together, which seemed to indicate an obvious GB migration from G2 to G1. However, as shown in Fig. 4(-d)-(f), G2 was more easily deformed and hence had a higher dislocation density than G1 according to the Taylor factor criterion (a soft crystalline orientation for G2 in essence) [32]. The higher average KAM value of G2 (0.26 for G1 and 0.35 for G2) further verified the larger strain and the corresponding higher dislocation density within G2 than G1. The nucleation of G3 and G4 mentioned above also confirmed the distribution differences of strain and dislocation density between G1 and G2. Therefore, the original GB between G1 and G2 should prefer to migrate and bulge towards G2 rather than G1, which, nevertheless, disagreed with the GB profile features around SG1. The theoretical migrating direction and actual bulging direction were opposite for the original GB in the nucleation process of SG1, which was very different from the DRX nucleation through the SIGBB mechanism.

A passive grain boundary bulging (PGBB) mechanism was proposed in this work to explain the nucleation process of SG1. The original grain boundaries B-C-E and A-D-F migrated and bulged towards the higher dislocation density grain G2 to form G3 and G4, i.e., nucleation through the typical SIGBB mechanism (Fig. 4(b)). In the meantime, the original GB fragment A-B lagged behind due to a relatively lower migration velocity, and hence passively bulged towards the opposite direction of its migration direction. Subsequently, the GB sliding easily led to shearing strain concentrations at points C and D, and consequently triggered the formation of grain boundary C-D. A clear transformation from subgrain boundaries to GBs was detected here, and a well-developed DRX grain formed when subgrain boundaries C-G and D-H both entirely evolved into GBs (Fig. 4(c)). Therefore, the PGBB mechanism operated well during the DRX nucleation process between the initial DRX nuclei formed by the SIGBB mechanism.

The PGBB model proposed above is a critical complement to the DRX nucleation mechanisms associated with the original GBs, which also accounts for the formation of the continuous necklace structure, instead of an interrupted one, during the early stage of DRX. As schematized in Fig. 5, fragments of one original GB migrate towards the grain with higher dislocation density at different velocities due to the various driving forces at each individual fragment. The fragment with a stronger driving force easily bulges along its migration direction, which then nucleated through the SIGBB mechanism. The fragment with a weaker driving force lags behind and hence passively bulges opposite its migration direction, although it is still migrating to the grain with a higher dislocation density (Fig. 5(a)). It must be distinguished from the features of GB migration during DRX nucleation through the SIGBB mechanism. The relative boundary sliding then generates shearing strain concentrations to trigger the formation of new boundaries to enclose the DRX nuclei (Fig. 5(b)-(d)). Obviously, the PGBB mechanism operates well on the original GB fragments between two fragments controlled by the SIGBB mechanism, which hence generates a continuous necklace structure (Fig. 5(e)).

3.1.3. Nucleation mechanism at 3-grain junctions

Three common faces, i.e., GBs in 2D CSs, and one common edge simplified as a line exists at a 3-grain junction, which easily lead to strain concentrations and correspondingly the severe dislocation accumulation at 3-grain junctions, as discussed in Section 3.1.1. A typical nucleation process at the junction of grains G1, G2 and G3 was frozen and preserved by timely quenching, which permitted a meticulous research on the nucleation mechanism operating there (Fig. 6). The mean KAM values of G1, G2 and G3 were measured to be 0.380, 0.413 and 0.414, and the TFs along CD direction of them were 2.46, 2.35 and 2.31, respectively (Fig. 6(a)). This result indicates a heterogeneous strain distribution among the three adjacent deformed grains, and naturally different dislocation densities (positively correlating to the KAM values here). The GB fragments between G1 and G3, i.e., fragments C-D and D-E, were hence driven to migrate and bulge out towards G3, which generated a micro area with no or few strains behind the two fragments (Fig. 6(b) and (c)). Subsequently, a new subgrain formed after this area was closed by the newborn subgrain boundary B-D. It can be concluded preliminarily that the strain-induced bulging of the GB fragments closely adjoining the 3-grain junction controlled the DRX nucleation at the junction. In the following, special attention was focused on the boundary motion to explore the underlying nucleation mechanisms operating at 3-grain junctions.

The newborn boundaries at this 3-grain junction in Fig. 6(b) were found to be roughly located along the extended lines of the other original GBs constituting the junction. Specifically, newborn grain boundary B-C and subgrain boundary A-B almost coincided with the extended lines of the original GB between grains G1 and G3, and also the newborn subgrain boundary B-D with the extended lines of the original GB between grains G2 and G3 (Fig. 6(b)). The shearing strain induced by GB sliding is responsible for this. As schematized in Fig. 7, dislocations accumulate around the 3-grain junction (marked by a grey area), and the dislocation densities of the three adjacent grains are different due to their individual crystal orientation (an increasing trend from G1 to G3 by assumption here). The great difference in dislocation density between G1 and G3 drives the GB fragment, which is close to the junction, of GB III to migrate and bulge towards the grain with the highest dislocation density, i.e., the grain G3 with the least TF value, to generate a strain-free volume (Fig. 7(a) and (b)). The strain-free volume exhibits the same crystal orientation as its parent grain G1 at this stage. A powerful driving force acting on the GB fragment between the strain-free volume and G2 will appear due to the distinct difference in dislocation density between them, which power this fragment to migrate and bulge to G2, as shown in Fig. 7(c). The strain-free volume hence evolves towards both G2 and G3, while the relative sliding between deformed grains induces shearing strain along the directions of the original GBs and then promotes the formation of the new subgrain boundaries, which closes the strain-free volume to generate DRX nuclei (Fig. 7(d) and (e)). Continuous dislocation movement and rearrangement control the evolution from subgrain boundaries to GBs and the transformation from DRX nuclei to DRX grains. The newborn subgrain boundary in Fig. 7(d) develops well due to the distinct difference in dislocation density between its sides, and hence migrates to engulf the parent deformed grain G1 gradually (Fig. 7(e) and (f)). The development of the newborn subgrain boundary marked by the dotted line in Fig. 7(e) is restrained for the low dislocation density within the DRX grain. In addition, there is no sufficient driving force for its migration because of the tiny difference in dislocation density at both sides of this subgrain boundary. Therefore,

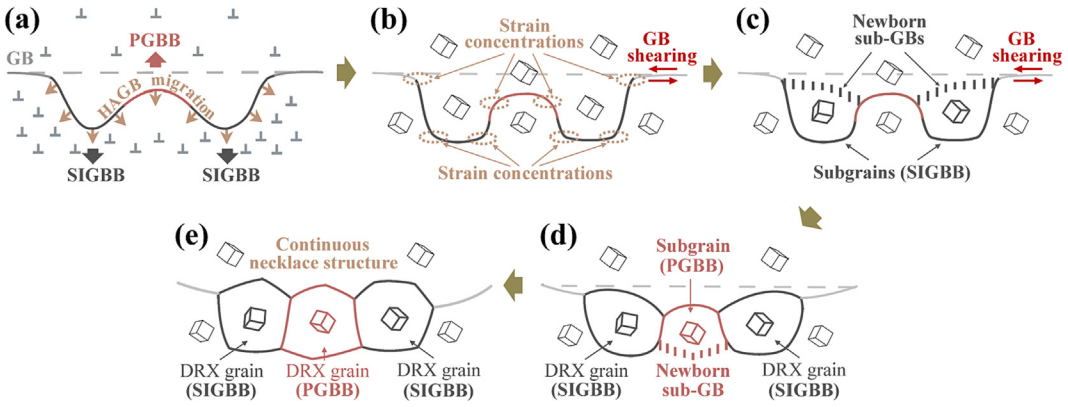

Fig. 5. Schematic diagrams of DRX nucleation at the 2-grain junction: (a) bulging processes of different GBFs, including PGBB and SIGBB; (b) strain concentration resulting from original GB shearing; (c) formation of subgrain boundaries behind SIGBB boundaries; (d) formation of subgrain boundaries behind PGBB boundaries; (e) continuous necklace structure formed through the combined operation of SIGBB and PGBB mechanisms.

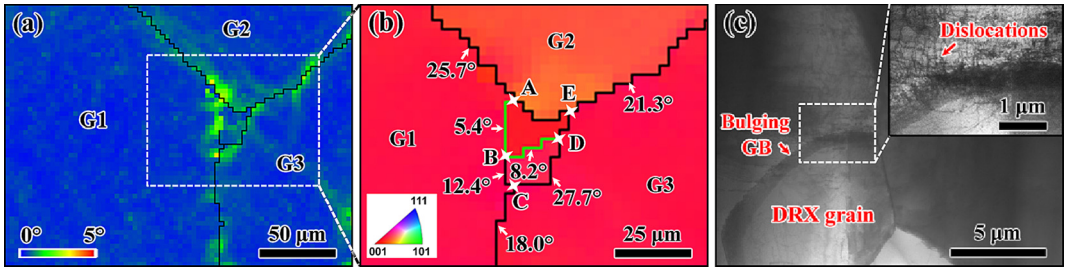

Fig. 6. DRX nucleation process captured at 3-grain junctions of GH4720Li type A samples compressed to a strain of 0.13 at 1140 °C with a strain rate of 0.1 s^{-1}: (a) KAM map; (b) OIM image along Z direction; (c) TEM image.

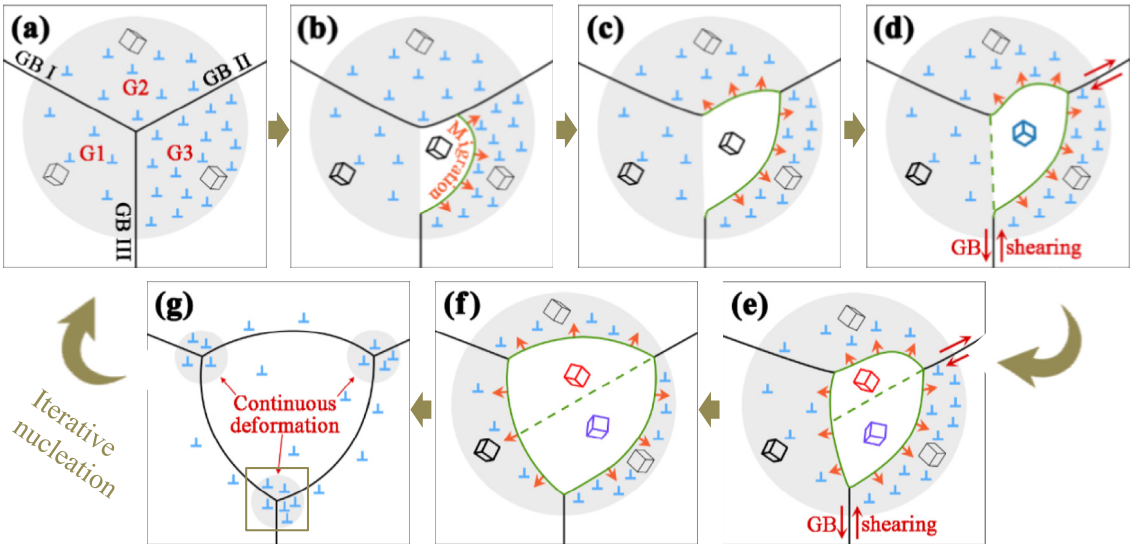

Fig. 7. Schematic of DRX nucleation at 3-grain junctions.

this subgrain boundary prefers to maintain a lower misorientation angle and a straight morphology at this stage. It should be noted that dislocation movement will be inevitably activated within the well-developed DRX grains during a continuous deformation process, and the dislocation density here will increase correspondingly (Fig. 7(g)). A similar nucleation as discussed above will be activated easily at the new 3-grain junctions consisting of original grains and the deformed DRX grains. This process can be referred to as an iterative nucleation process, which helps to account for the process that DRX grains engulf and replace the deformed grains gradually.

3.2. DRX nucleation priorities based on thermodynamics

Higher strain concentrations take place around grain junctions when a polycrystalline superalloy is deformed, which provides the necessary driving force to preferentially activate DRX nucleation. The results in Section 3.1 indicate a higher DRX nucleation

priority at 3-grain junctions than at 2-grain junctions, and the thermodynamic method is used to explain this in the following. The nucleation priority of 4-grain junctions, which is hard to be captured during microstructure characterization, will be also discussed. Because GB movement controls the DRX nucleation at grain junctions, the classical nucleation theory derived from phase transformations can describe the DRX nucleation process there after a modification [33]:

$$\Delta G = \Delta G_1 + \Delta G_2 \tag{1}$$

where the first term represents the variation of interfacial energy, and the second term represents the decrease of deformation stored energy during DRX nucleation.

The eliminated GB area between deformed grains during DRX nucleation at grain junctions can be given by

$$A_{Def/Def} = ar^2 \tag{2}$$

The increasing GB area can be written as

$$A_{Def/New} = br^2 \tag{3}$$

The volume of new DRX nucleus is

$$V = cr^3 \tag{4}$$

where a, b and c are coefficients depending on the GB energy, and r is the radius of curvature of the surfaces bounding the new DRX nucleus [34].

It is assumed that the stored deformation energy is released entirely after the migration of GBs. On the basis of Eqs. (2), (3) and (4), Eq. (1) can be rewritten as follows:

$$\Delta G = \sigma_{Def/New} \cdot br^2 - \sigma_{Def/Def} \cdot ar^2 - E_s \cdot cr^3 \tag{5}$$

where $\sigma_{Def/New}$ and $\sigma_{Def/Def}$ are the interfacial energy values between deformed grain and DRX nucleus, as well as deformed grains, respectively. E_s represents the stored deformation energy per unit volume.

For a given nucleation process, $\sigma_{Def/New}$, $\sigma_{Def/Def}$, E_s, as well as coefficients a, b and c are all constant. Therefore, ΔG is a function of r, and the critical nucleus radius can be calculated:

$$\frac{\partial \Delta G}{\partial r} = 2br \cdot \sigma_{Def/New} - 2ar \cdot \sigma_{Def/Def} - 3cr^2 \cdot E_s = 0 \tag{6}$$

It can be rewritten as follows:

$$r^* = \frac{2}{3} \cdot \frac{b\sigma_{Def/New} - a\sigma_{Def/Def}}{c \cdot E_s} \tag{7}$$

With the combination of Eqs. (5) and (7), the critical activation energy for DRX nucleation at grain junctions is determined as:

$$\Delta G^* = \frac{4}{27} \cdot \frac{\left(b\sigma_{D/N} - a\sigma_{D/D}\right)^3}{c^2 {E_s}^2} \tag{8}$$

Prior investigations indicate that there is no certain relationship between the energy and misorientation angle of random grain boundaries [15]. Therefore, the original GBs are reasonably supposed to have the same energy as the newborn GBs in consideration of the same crystal lattice structure between the original grains and the DRX nuclei, namely, $\sigma_{Def/Nef} = \sigma_{Def/DRX} = \sigma$. On this basis, Eq. (8) can be rewritten as:

$$\Delta G^* = \frac{4}{27} \cdot \frac{\sigma^3}{E_s^2} \cdot \frac{(b-a)^3}{c^2} \tag{9}$$

Adapting from the calculation during solid transformations proposed by P.J. Clemm and J.C. Fisher [34], a, b and c at different types of DRX nucleation sites can be determined as follows:

(I) for 2-grain junctions:

$$\begin{cases} a = \pi\left(1-k^2\right) \\ b = 4\pi(1-k) \\ c = \frac{2\pi}{3}\left(2-3k+k^3\right) \end{cases} \tag{10}$$

(II) for 3-grain junctions:

$$\begin{cases} a = 3\beta\left(1-k^2\right) - k\left(3-4k^2\right)^{\frac{1}{2}} \\ b = 12\left(\frac{\pi}{2} - \alpha - k\beta\right) \\ c = 2\left[\pi - 2\alpha + \frac{k^2}{3}\left(3-4k^2\right)^{\frac{1}{2}} - \beta k\left(3-k^2\right)\right] \end{cases} \tag{11}$$

(III) for 4-grain junctions:

$$\begin{cases} a = 3\left\{2\phi\left(1-k^2\right) - K\left[\left(1-k^2-\frac{K^2}{4}\right)^{\frac{1}{2}} - \frac{K^2}{\sqrt{8}}\right]\right\} \\ b = 24\left(\frac{\pi}{3} - k\phi - \delta\right) \\ c = 2\left\{4\left(\frac{\pi}{3}-\delta\right) + kK\left[\left(1-k^2-\frac{K^2}{4}\right)^{\frac{1}{2}} - \frac{K^2}{\sqrt{8}}\right] - 2k\phi\left(3-k^2\right)\right\} \end{cases} \tag{12}$$

where

$$k = cos\theta = \frac{\sigma_{D/D}}{2\sigma_{D/N}} \tag{13}$$

$$\alpha = sin^{-1}\frac{1}{2\left(1-k^2\right)^{\frac{1}{2}}} \tag{14}$$

$$\beta = cos^{-1}\frac{k}{\left[3\left(1-k^2\right)\right]^{\frac{1}{2}}} \tag{15}$$

$$K = \frac{4}{3}\left(\frac{3}{2} - 2k^2\right)^{\frac{1}{2}} - \frac{2}{3}k \tag{16}$$

$$\phi = sin^{-1}\frac{K}{2\left(1-k^2\right)^{\frac{1}{2}}} \tag{17}$$

$$\delta = cos^{-1}\frac{\sqrt{2} - k\left(3-K^2\right)^{\frac{1}{2}}}{K\left(1-k^2\right)^{\frac{1}{2}}} \tag{18}$$

By combining Eqs. (9)-(18), the critical activation energy for DRX nucleation at 2-, 3- and 4-grain junctions can be confirmed as follows:

(I) for 2-grain junctions:

$$\Delta G_{2gj}{}^* = \frac{4}{27} \cdot \frac{\sigma^3}{E_s^2} \cdot \frac{(b-a)^3}{c^2} = 5.24 \cdot \frac{\sigma^3}{E_{s1}^2} \tag{19}$$

(II) for 3-grain junctions:

$$\Delta G_{3gj}{}^* = \frac{4}{27} \cdot \frac{\sigma^3}{E_s^2} \cdot \frac{(b-a)^3}{c^2} = 2.69 \cdot \frac{\sigma^3}{E_{s2}^2} \tag{20}$$

(III) for 4-grain junctions:

$$\Delta G_{4gj}{}^* = \frac{4}{27} \cdot \frac{\sigma^3}{E_s^2} \cdot \frac{(b-a)^3}{c^2} = 1.69 \cdot \frac{\sigma^3}{E_{s3}^2} \tag{21}$$

where E_{s1}, E_{s2} and E_{s3} represent the stored deformation energy per unit volume around 2-, 3- and 4-grain junctions respectively, and the values of them certainly increase one by one in consideration

of the strain concentration around grain junctions discussed in Section 3.1, i.e.,

$$E_{s1} < E_{s2} < E_{s3} \tag{22}$$

By combining Eqs. (19)-(22), the critical activation energy for DRX nucleation at 2-, 3- and 4-grain junctions can be ranked as follows:

$$5.24 \cdot \frac{\sigma^3}{E_{s1}^2} > 5.24 \cdot \frac{\sigma^3}{E_{s2}^2} > 2.69 \cdot \frac{\sigma^3}{E_{s2}^2} > 2.69 \cdot \frac{\sigma^3}{E_{s3}^2} > 1.69 \cdot \frac{\sigma^3}{E_{s3}^2} \tag{23}$$

It can be rewritten as follows:

$$\Delta G_{2gj}{}^* > \Delta G_{3gj}{}^* > \Delta G_{4gj}{}^* \tag{24}$$

Therefore, the critical activated energy for DRX nucleation obviously decreased in the order from 2-, 3- to 4-grain junctions. This result indicates the highest DRX nucleation priority at 4-grain junctions, followed by 3-grain junctions and finally the 2-grain junctions during the hot deformation process studied in the present manuscript.

3.3. Orientation dependence of DRX nucleation

3.3.1. DRX nucleation at 2-grain junctions

Fig. 8 shows the microstructure of GH4720Li type B samples compressed to a strain of 0.69 at 1140 °C with a strain rate of 0.1 s^{-1}. These fine grains were identified as DRX grains with an average equivalent diameter of 14.05 μm. All DRX grains evolved and distributed along original GBs in the form of necklace structures or fine grain bands. It was worth noting that the amount of DRX grains was very different at each individual original GB, even at each GB fragment. As shown in Fig. 8(a), the necklace structure replaced the original GBs, and some of them developed into DRX bands, which indicated a quite well-developed DRX microstructure in these microareas. However, original GBs with no or few DRX grains could be still detected, although the volume fraction of DRX grains was measured to be 49.2%, such as GB fragments I and II marked in Fig. 8(a). It indicated that not all original GBs were appropriate for DRX nucleation despite the critical role GBs played during the DRX process.

A rule of DRX nucleation was found when one focused on the Taylor factor (CD, {1 1 1} ⟨1 1 0⟩) distribution of the microstructure. As shown in Fig. 8(b), the well-developed DRX bands occurred between the deformed grains with very different Taylor factors (TFs), such as grains G3 and G4, as well as G6 and G7. The average TFs of the four grains were measured to be 2.38, 3.61, 3.57 and 2.41. DRX grains seemed to preferentially nucleate at the original GBs between these deformed grains, and subsequently formed DRX bands to replace the GBs. On the contrary, no or few DRX grains occurred at the original GBs between grains with similar TFs, such as GB fragments I and II (Fig. 8(a)). The average TFs of 20 μm-wide bands along both sides of GB fragment I were measured to be 2.67 and 2.39, and those along both sides of GB fragment II were 2.40 and 2.39. The tiny differences in TFs on both sides of the two GB fragments corresponded to the repressed DRX nucleation and the delayed microstructure evolution there during hot deformation. Obviously, the differences between adjacent grains' TFs strongly affected the DRX nucleation behaviors at the original GBs between these grains. The original GBs consisting of grains with very different TFs exhibited higher nucleation prior-

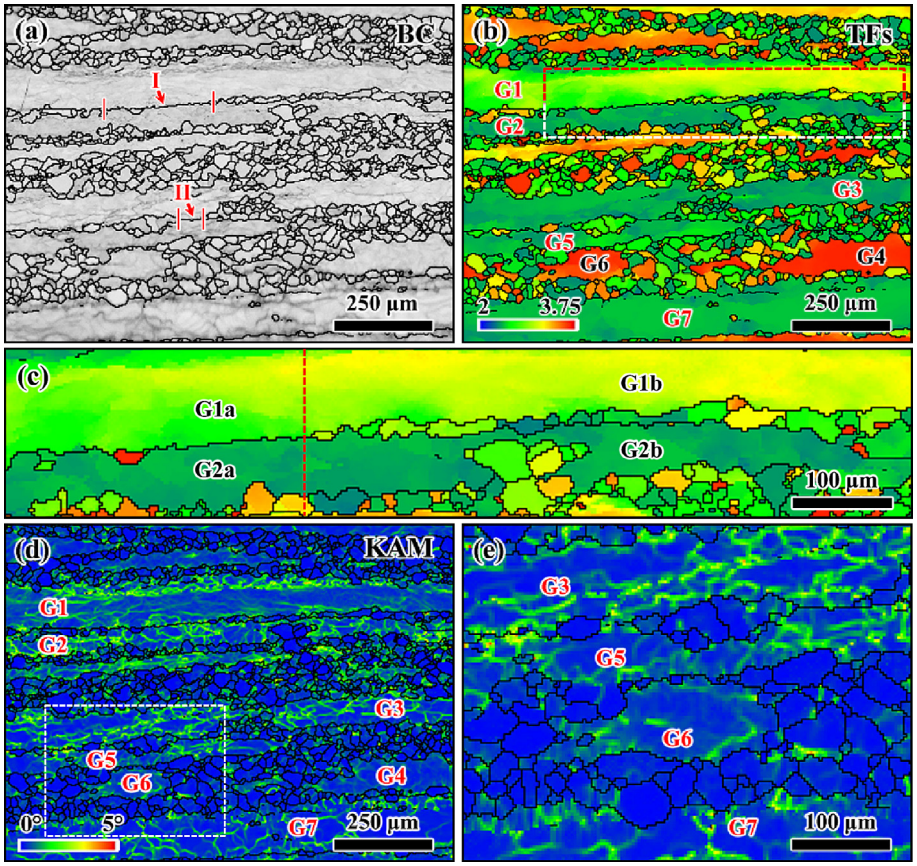

Fig. 8. Microstructures of GH4720Li type B samples compressed to a strain of 0.69 at 1140 °C with a strain of 0.1 s^{-1}: (a) band contrast image; (b) Taylor factor distribution along CD direction; (c) magnification of the rectangular region in (b); (d) KAM map; (e) magnification of the rectangular region in (d).

ities. DRX grains preferred to nucleate at these GBs and easily evolved into DRX bands, while no or few DRX grains occurred at the original GBs consisting of grains with similar TFs.

The distinctive DRX behaviors at different fragments of one original GB would be further evidence of the above conclusion. As shown in Fig. 8(c), deformed grains G1 and G2 were divided into different microareas by a dotted line. For a simplification of description, the original GB between the two grains was also divided into two parts, which were titled GB fragments G1a-2a and G1b-2b. GB bulging could be detected at fragment G1a-G2a, and only several DRX grains formed. It indicated that DRX nucleation had been activated there but was sluggish, and the process was hence frozen by water quenching before more nuclei formed. In comparison, DRX nucleation seemed to be easier and quicker at fragment G1b-G2b, where more DRX grains occurred at the same deformation process. Finally, a well-developed necklace structure formed between microareas G1b and G2b, and the original GB fragment here was entirely replaced. The TF differences between the two sides of fragments G1a-G2a and G1b-G2b were 0.34 and 0.53. Obviously, the GB bulging mechanism preferred to be activated first at the fragment with larger Taylor factor difference, rather than that with the less one, which coincided with the nucleation rule at original GBs discussed above.

The driving force, temperature and strain rate, i.e., the time for nucleation and grain growth in essence, strongly affected the DRX behavior during hot deformation [14,35]. The temperature almost distributed uniformly around adjacent GBs or different GB fragments of one GB, and the time was constant for a given deformation process. The tiny differences in temperature and time between adjacent GBs or GB fragments resulting from the quenching process could not generate the obvious and regular heterogeneous distribution of DRX grains discussed above. Attention was hence focused on the driving force to understand the distinct DRX nucleation priority at GBs or GB fragments with different Taylor factor differences, as well as the consequently heterogeneous distribution of DRX grains. Taylor factor is the geometric factor that measures the influence of a grain's lattice orientation on its resistance to deformation [36,37]. Local stress equilibrium between adjacent grains must be established to accommodate deformation, and the grain with lower TFs behaved as the soft grain to deform more easily than the grain with higher TFs [32]. Therefore, the grains with lower TFs (G1, G2, G3, G5 and G7 in Fig. 8(b)) activated slip systems to yield and deform more easily than the grains with higher TFs (G4 and G6 in Fig. 8(b)), which affected the strain distribution and the dislocation densities within these grains. The average KAM values, which were proportional to dislocation density at a constant scanning step [38], of G1-G7 were measured to be 0.74, 0.92, 0.71, 0.47, 0.61, 0.56 and 0.45, respectively (Fig. 8(d) and (e)). There was a marked difference in dislocation density between G3 and G4, as well as G6 and G7, which drove the original GBs between them to bulge towards the deformed grain with higher dislocation density and then nucleated. The well-developed necklace structures formed there and finally evolved into DRX bands. For the original GBs consisting of grains both with lower TFs (G1 and G2, as well as G3 and G5), although there were higher dislocation densities within these grains, the tiny difference in dislocation densities between adjacent grains meant weaker driving forces for GB migration and bulging, and the DRX nucleation was hence restrained.

3.3.2. DRX nucleation at 3-grain junctions

Fig. 9 shows the microstructures of GH4720Li type A samples compressed to a strain of 0.13 at 1140 °C with a strain rate of 0.1 s^{-1}. The microstructure evolution processes at 3-grain junctions were captured well by the utilization of original columnar grains, the optimized deformation parameters and the CSs perpendicular to the columnar grain growth direction. Very different DRX behaviors could be found at the three adjacent 3-grain junctions, which were marked by ellipses I, II and III. The fine grains G6, G7, G8 and G9 at 3-grain junction I, as well as the fine grains G10 and G11 at 3-grain junction II, were all identified as DRX grains according to their low strain and morphology features. Distinct GB bulging could be observed near 3-grain junction III but no DRX grain occurred. DRX processes developed well at these 3-grain junctions which consisted of the original grains with very different TFs, rather than at those consisting of grains with similar TFs (Fig. 9 (b)). This meant a higher nucleation priority for the former, which was attributed to the crystal orientation of the component grains of junctions. As discussed in Section 3.1.3, the motion of GB fragments which closely adjoined the 3-grain junction controlled the DRX nucleation at the junctions. It was the dislocation density differences between the sides of the GB fragments that drove the fragments to migrate and bulge. Grains G1 and G3 with lower TFs exhibited lower deformation resistance and hence deformed more easily, which was accompanied by the higher dislocation densities and correspondingly the higher KAM values (0.59 and 0.44, respectively). In contrast, plastic deformation was hard for G2 due to the larger deformation resistance which resulted from the hard lattice orientation represented by a higher Taylor factor. A KAM value of 0.36 within G2 proved a much lower dislocation density than G1 and G3, which induced the bulging of the GB fragments closely adjoining 3-grain junction I and consequently activated the DRX nucleation here. The same mechanism also operated well at 3-grain junction II, which was composed of deformed grains G2, G3 and G5. For 3-grain junction III, the component grains G1, G3 and G4 possessed similar TFs (0.59, 0.44 and 0.40, respectively) and KAM values (2.35, 2.49 and 2.50, respectively). Tiny difference in dislocation densities among G1, G3 and G4 restrained the migration of GBs due to insufficient driving force and hence delayed the nucleation at junction III. In summary, the nucleation priority of each individual 3-grain junction was significantly affected by the crystal orientation of its component deformed grains, which could be quantized by the difference in TFs among the component grains. The more marked the differences mentioned above were, the higher DRX nucleation priority the 3-grain junction would exhibit under given deformation conditions.

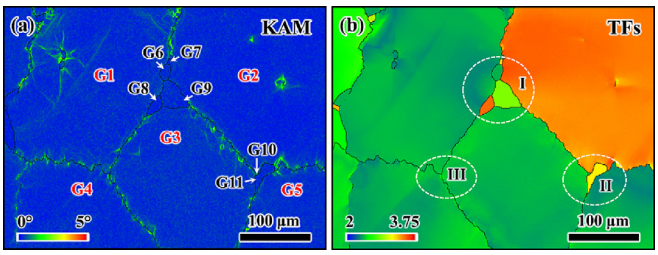

Fig. 9. Microstructure of GH4720Li type A samples compressed to a strain of 0.13 at 1140 °C with a strain rate of 0.1 s^{-1}: (a) KAM map; (b) Taylor factor distribution along CD direction.

A larger deformed area (1420 × 1062 μm) within the same sample, including more 3-grain junctions, was examined to supply statistical data to verify the conclusion obtained above. Standard deviation (SD) was used to estimate and quantify the differences in TFs among three adjacent grains to explore the effect of component grains' orientations on DRX nucleation behavior at 3-grain junctions. As shown in Table 2, one/no subgrain was detected at the 3-grain junctions with Taylor factor SD values lower than 0.14 under the given deformation condition. No well-developed DRX grain formed at these junctions due to the limited driving force for GB migration, although there might be quite a few strain concentrations. For the 3-grain junctions with Taylor factor SD val-

Table 2
Influence of Taylor factor SD values among three component grains on DRX nucleation.

No.	TFs of component grains			SD of TFs	DRX grain number	
	Grain 1	Grain 2	Grain 3		Subgrain	Grain
1	2.4743	2.3640	2.4006	0.0562	1	0
2	2.3597	2.4876	2.5043	0.0791	1	0
3	2.5744	2.7050	2.7426	0.0882	0	0
4	2.5241	2.6693	2.4949	0.0934	1	0
5	2.7050	2.5241	2.7426	0.1168	0	0
6	2.3597	2.3328	2.5744	0.1324	1	0
7	2.5241	2.4949	2.7426	0.1353	1	0
8	2.7426	2.9929	2.9598	0.1359	1	1
9	2.3640	2.6277	2.4006	0.1428	2	0
10	2.3597	2.5744	2.7050	0.1743	0	1
11	2.5744	2.7426	2.9927	0.2105	2	2
12	2.4949	3.6262	3.2511	0.5763	0	2
13	2.4876	3.5175	2.4743	0.5984	0	2
14	2.6693	2.4949	3.6262	0.6091	0	4
15	2.3597	2.4876	3.5175	0.6347	0	3
16	3.5175	2.4743	2.3640	0.6365	0	2
17	3.5175	2.3640	2.4169	0.6512	0	2
18	3.5175	2.4169	2.3631	0.6515	3	1
19	3.5175	2.3631	2.3328	0.6754	2	2

ues higher than 0.57, at least two or more DRX grains/subgrains formed. This result coincided with the conclusion obtained above that the more marked the differences among three component grains' TFs were, the higher DRX nucleation priority at the 3-grain junctions was.

3.4. Microstructure evolution associated with grain junctions

3D observation through the microstructure characterization of serial CSs helps to study the microstructure evolution at 2- and 3-grain junctions during hot deformation (Fig. 2). Fig. 10 shows the microstructures of five serial CSs obtained at one projection area, and the 2-grain junction between grains G1 and G2 deserves special attention. GB bulging could be observed within the ellipse area, but no well-developed DRX grain was detected on the first CSs (Fig. 10(a)). Four DRX grains were detected to develop well and adjoined each other on the second CSs (Fig. 10(b)). The number and the area of DRX grains continued to increase on the third CSs, which almost generated a well-developed necklace structure here (Fig. 10(c)). Fig. 10(d) and (e) indicated that the number and the area of DRX grains gradually decreased. By combining the microstructure features on the five CSs, a thin cake-shaped DRX volume in 3D could be confirmed on this 2-grain junction between G1 and G2 (Fig. 10(f)). In summary, DRX grains tend to nucleate around the first nucleus layer by layer on this face first, which forms a thin cake consisting of DRX grains between the two deformed grains. In addition, in consideration of the effect of dislocation density, the DRX grains here prefer to engulf the one deformed grain with higher TFs to grow up, which easily generated a hump on the thin cake.

Fig. 11 shows the microstructure on five serial CSs obtained from the same projection area of one type A sample. The amount and morphology of DRX grains around the 3-grain junctions varied with the locations of CSs but never faded away. DRX grains on all CSs distributed along the GBs adjoining the 3-grain junctions, and no DRX grains nucleated at the interiors of deformed grains

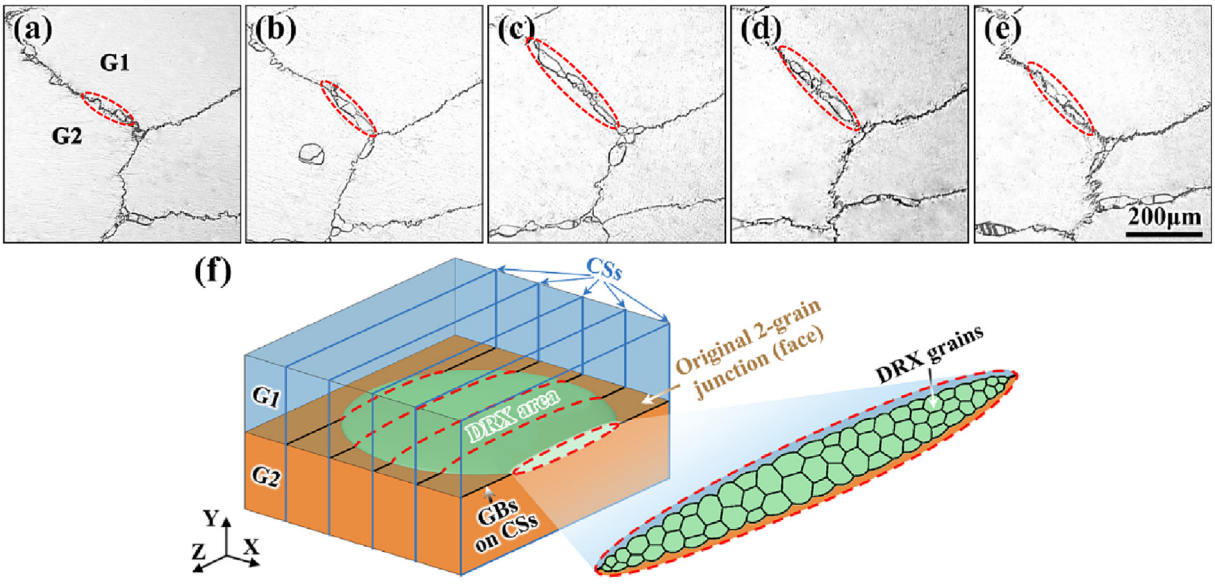

Fig. 10. DRX grains at the original 2-grain junctions captured on CSs of type A samples deformed at 1140 °C with a strain rate of 0.1 s^{-1}: (a)-(e) serial CSs numbered from 1 to 5; (f) 3D schematic of DRX grain distribution on the original 2-grain junction.

or even nucleated beside GBs to evolve towards the interior of deformed grains. DRX nucleation tended to form at the GBs adjoining the 3-grain junctions after the latter were engulfed by DRX grains, instead of developing directly into the interior of deformed grains, which indicated a decreasing nucleation priority in an order from 3-, 2-grain junctions to the interiors of deformed grains. The

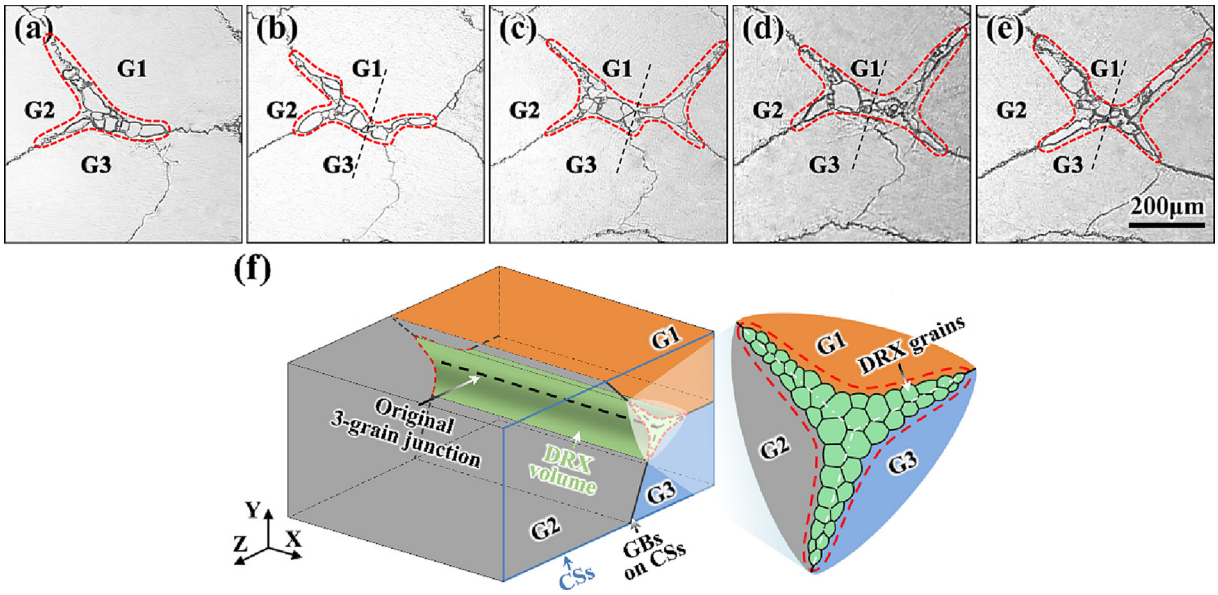

Fig. 11. DRX grains at the original 3-grain junctions captured on five CSs of type A samples deformed at 1140 °C with a strain rate of 0.1 s^{-1}: (a)-(e) serial CSs numbered from 1 to 5; (f) 3D schematic of DRX grain distribution at the original 3-grain junction.

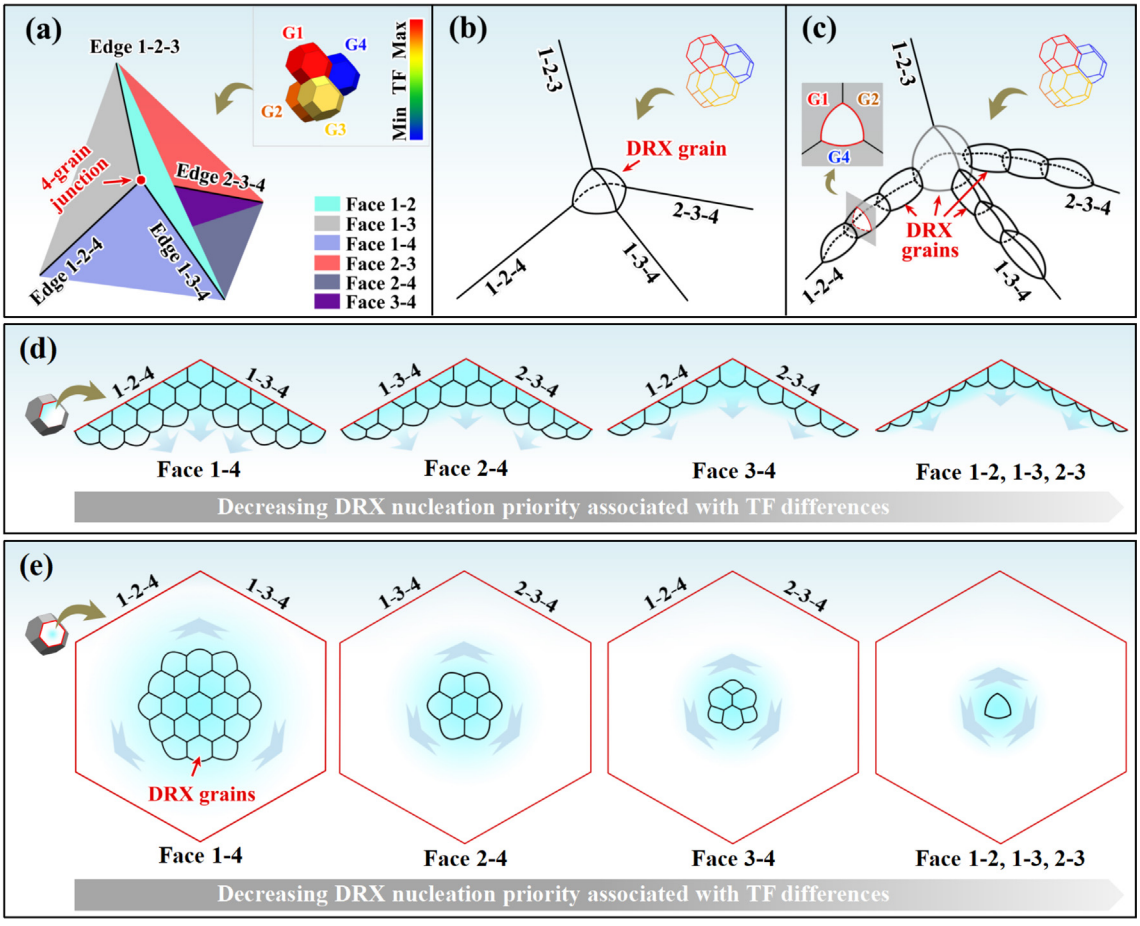

Fig. 12. Schematic of microstructure evolution for a 4-grain stacking unit including 2-, 3- and 4-grain junctions: (a) 4-grain stacking unit and labeling of junctions; (b)-(e) DRX microstructure evolution at 4- and 3-grain junctions, as well as the 2-grain junctions next to the edges and far from the edges, respectively.

DRX areas hence showed X shapes, marked by dotted lines, around one 3-grain junction on CSs before the deformed structures were entirely replaced (Fig. 11(a)-(e)). It meant that the DRX volume along 3-grain junction in 3D space was roughly an aberrant triangular prism with concave side faces, as shown in Fig. 11(f).

Based on the prior discussion in the manuscript, the microstructure evolution for a 4-grain stacking unit including 2-, 3- and 4-grain junctions can be confirmed. Fig. 12(a) is the schematic diagram for the stacking unit consisting of four grains. The TFs of the four component grains decrease from G1 to G4, and relatively smaller differences in TFs are assumed among G1, G2 and G3. In addition, face 1–2 refers to the 2-grain junction consisting of G1 and G2 for convenience, while edge 1–2–3 refers to the 3-grain junction consisting of G1, G2 and G3. The remaining grain junctions are all titled in the same manner. For the 4-grain stacking unit, DRX nucleation is first activated at the 4-grain junction consisting of G1, G2, G3 and G4 due to its lowest critical activation energy for nucleation (Section 3.2), as shown in Fig. 12(b). In consideration of the effect of crystal orientation on deformation accommodation and strain distribution, the newborn DRX grain here prefers to grow up towards G4 due to the lowest deformation resistance and hence the highest dislocation density of G4. The 3-grain junctions are the second-best DRX nucleation site because of the lower critical activation energy after 4-grain junctions. As shown in Fig. 12(c), DRX nucleation was delayed at edge 1–2–3 due to the similar TFs among G1, G2 and G3, while the marked differences in TFs at edge 1–2–4, edge 1–3–4 and edge 2–3–4 benefit GB migration and hence accelerate DRX nucleation here. DRX grains tend to develop along edges 1–2–4, 1–3–4 and 2–3–4 to gradually engulf the 3-grain junctions. Subsequently, DRX nucleation is activated at 2-grain junctions because of the higher critical activation energy for nucleation than that at 3- and 4-grain junctions. The dislocation density differences between both sides of the 2-grain junctions here decrease gradually in the order of faces 1–4, 2–4, 3–4, 1–3, 1–2, and 2–3. Therefore, DRX grains tend to nucleate on the faces between deformed grains in the order above after the 3-grain junctions were engulfed by DRX grains. Two situations are classified into two types according to the location of DRX grains on the faces. First, DRX grains nucleate next to the DRX grains which previously nucleated at 3-grain junctions on the faces (Fig. 12(d)). The Y-shaped DRX areas can hence be observed on the CSs perpendicular to the direction of the 3-grain junctions before the deformed structures were entirely replaced. Second, DRX nucleation are activated on the faces far from the edges, provided that the component grains of the 2-grain junctions possess very different TFs, such as face 1–4 (Fig. 12(e)). In this case, new DRX grains prefer to nucleate around the first one to spread on the faces, rather than develop towards the interiors of deformed grains directly. It hence results in a pancake-like DRX area between deformed grains until the faces are replaced by DRX grains.

4. Conclusions

The original grain junctions closely relate to the DRX of polycrystalline nickel-based superalloys owing to the lower SFE. In this manuscript, DRX nucleation process at 2-, 3- and 4-grain junctions of GH4720Li superalloy was investigated with special attentions focused on the nucleation priorities, the nucleation mechanisms and the orientation dependence of nucleation at these grain junctions. Subsequently, the DRX microstructure evolution tendency of a 4-grain stacking unit was then confirmed by considering the factors discussed previously. These works made it possible to better understand the microstructure evolution considering the multiple grain junctions during the hot deformation, and finally to effectively tailor microstructures to match the property requirements of turbine disk forgings. The following conclusions can be drawn from this study:

(1) A PGBB mechanism was proposed to explain the DRX nucleation between the DRX grains which previously nucleated through SIGBB. It was a critical complement to the DRX nucleation mechanisms associated with GBs, which also accounted for the formation of the continuous necklace structure, instead of an interrupted one, during the early stage of DRX.
(2) A two-step strain-induced bulging of the GB fragments closely adjoining 3-grain junctions dominated the DRX nucleation at these junctions. The GB shearing triggered the formation of new subgrain boundaries and the DRX nuclei.
(3) The DRX nucleation priorities of the same kind of grain junctions strongly depended on the orientation of the component grains and can be estimated by their TFs. The larger the difference value of TFs between two adjacent grains was, the higher nucleation priority of the 2-grain junction would be under a given deformation condition. The same rule applied to the estimation for nucleation priority of the 3-grain junctions, provided that the SD values of TFs among their component grains were used.
(4) The DRX nucleation priorities of the 2-, 3- and 4-grain junctions were confirmed both by microstructure characterization and thermodynamic method. For a 4-grain stacking unit of polycrystalline superalloys, DRX grains nucleated first at the 4-grain junction, and then at its adjacent 3-grain junctions with larger Taylor factor differences. The 2-grain junctions exhibited lower nucleation priority by comparison, and DRX grains nucleated on the faces where next to the 3-grain junctions or where far from the edges.

CRediT authorship contribution statement

Bingchao Xie: Conceptualization, Methodology, Validation, Investigation, Writing – original draft, Writing – review & editing. **Heng Li:** Methodology, Validation, Methodology, Writing – review & editing, Supervision. **Yongquan Ning:** Conceptualization, Investigation, Data curation, Project administration, Writing – review & editing, Supervision, Resources. **Mingwang Fu:** Conceptualization, Supervision, Writing – review & editing.

Data availability

Data will be made available on request.

Declaration of Competing Interest

The authors declare that they have no known competing financial interests or personal relationships that could have appeared to influence the work reported in this paper.

Acknowledgements

The work was financially supported by the China Postdoctoral Science Foundation [grant numbers 2022M722589]; the Natural Science Foundation of Shaanxi Province of China [grant numbers 2023-JC-QN-0466]; and the National Natural Science Foundation of China [grant numbers 52175363].

References

[1] C. Panwisawas, Y.T. Tang, R.C. Reed, Metal 3D printing as a disruptive technology for superalloys [J], Nat. Commun. 11 (2020) 1–4, https://doi.org/10.1038/s41467-020-16188-7.

[2] X.F. Dang, Y. Li, K. Chen, S.H. Luo, X.Q. Liang, W.F. He, Insight into the interfacial architecture of a hybrid additively- manufactured stainless steel/Ni-based superalloy bimetal [J], Mater. Des. 216 (2022), https://doi.org/10.1016/j.matdes.2022.110595 110595.
[3] A. Jena, S.E. Atabay, A. Gontcharov, P. Lowden, M. Brochu, Laser powder bed fusion of a new high gamma prime Ni-based superalloy with improved weldability [J], Mater. Des. 208 (2021), https://doi.org/10.1016/j.matdes.2021.109895 109895.
[4] N.R. Jaladurgam, S. Kabra, M.H. Colliander, Macro- and micro-mechanical behaviour of a γ′ strengthened Ni-based superalloy at cryogenic temperatures [J], Mater. Des. 209 (2021), https://doi.org/10.1016/j.matdes.2021.109954 109954.
[5] S. Utada, R. Sasaki, R.C. Reed, Y.T. Tang, Overheating of Waspaloy: Effect of cooling rate on flow stress behavior [J], Mater. Des. 221 (2022), https://doi.org/10.1016/j.matdes.2022.110911 110911.
[6] M.J. Wang, C.Y. Sun, M.W. Fu, Z.L. Liu, C.H. Wang, Microstructure and microtexture evolution of dynamic recrystallization during hot deformation of a nickel-based superalloy [J], Mater. Des. 188 (2020), https://doi.org/10.1016/j.matdes.2019.108429 108429.
[7] M. Shahwaz, P. Nath, I. Sen, A critical review on the microstructure and mechanical properties correlation of additively manufactured nickel-based superalloys [J], J. Alloy. Compd. 907 (2022), https://doi.org/10.1016/j.jallcom.2022.164530 164530.
[8] P.H. Geng, G.L. Qin, J. Zhou, T.Y. Li, N.S. Ma, Characterization of microstructures and hot-compressive behavior of GH4169 superalloy by kinetics analysis and simulation [J], J. Mater. Process. Tech. 288 (2021), https://doi.org/10.1016/j.jmatprotec.2020.116879 116879.
[9] L.L. Chen, H.N. Ding, T. Liu, R. Luo, Y. Cao, Y.X. Zhang, Y. Liu, F. Yuan, Y. Qiu, S.G. Cui, Y. Cao, X.N. Cheng, Thermal deformation behavior and microstructure evolution of GH4169 superalloy under the shear-compression deformation conditions [J], Mater. Des. 212 (2021), https://doi.org/10.1016/j.matdes.2021.110195 110195.
[10] Y.L. Zhu, Y. Cao, Q.B. He, R. Luo, J.K. Zhang, H.S. Di, G.J. Huang, Q. Liu, J. Xiao, Machine learning neural-network identification for dynamic recrystallization grains during hot deformation of nickel-based superalloy [J], Mater Charact 191 (2022), https://doi.org/10.1016/j.matchar.2022.112108 112108.
[11] D.H. Liu, H.R. Chai, L. Yang, W.Q. Qiu, Z.H. Guo, Z.L. Wang, Study on the dynamic recrystallization mechanisms of GH5188 superalloy during hot compression deformation [J], J. Alloy. Compd. 895 (2022), https://doi.org/10.1016/j.jallcom.2021.162565 162565.
[12] R. Luo, L.L. Chen, Y.X. Zhang, Y. Cao, C.T. Peng, Y.Y. Yang, T. Liu, Q. Zheng, X.N. Cheng, Characteristic and mechanism of dynamic recrystallization in a newly developed Fe-Cr-Ni-Al-Nb superalloy during hot deformation [J], J. Alloy. Compd. 865 (2021), https://doi.org/10.1016/j.jallcom.2021.158601 158601.
[13] P. Liu, R. Zhang, Y. Yuan, C.Y. Cui, F.G. Liang, X. Liu, Y.F. Gu, Y.Z. Zhou, X.F. Sun, Microstructural evolution of a Ni-Co based superalloy during hot compression at γ′ sub-/super-solvus temperatures [J], J. Mater. Sci. Technol. 77 (2021) 66–81, https://doi.org/10.1016/j.jmst.2020.10.042.
[14] H.K. Zhang, H. Xiao, X.W. Fang, Q. Zhang, R.E. Logé, K. Huang, A critical assessment of experimental investigation of dynamic recrystallization of metallic materials [J], Mater. Des. 193 (2020), https://doi.org/10.1016/j.matdes.2020.108873 108873.
[15] F.J. Humphreys, M. Hatherly, in: Recrystallization and Related Annealing Phenomena, Elsevier, 2004, pp. 91–119.
[16] G.D. Zhao, X.M. Zang, Y. Jing, N. Lü, J.J. Wu, Role of carbides on hot deformation behavior and dynamic recrystallization of hard-deformed superalloy U720Li [J], Mater. Sci. Eng. A 815 (2021), https://doi.org/10.1016/j.msea.2021.141293 141293.
[17] L.X. Ouyang, R. Luo, Y.W. Gui, Y. Cao, L.L. Chen, Y.J. Cui, H.K. Bian, K. Aoyagi, K. Yamanaka, A. Chiba, Hot deformation characteristics and dynamic recrystallization mechanisms of a Co–Ni-based superalloy [J], Mater. Sci. Eng. A 788 (2020), https://doi.org/10.1016/j.msea.2020.139638 139638.
[18] M.J. Wang, C.Y. Sun, M.W. Fu, Z.L. Liu, L.Y. Qian, Study on the dynamic recrystallization mechanisms of Inconel 740 superalloy during hot deformation [J], J. Alloy. Compd. 820 (2020), https://doi.org/10.1016/j.jallcom.2019.153325 153325.
[19] Y.J. Li, Y. Zhang, Z.Y. Chen, Z.C. Ji, H.Y. Zhu, C.F. Sun, W.P. Dong, X. Li, Y. Sun, S. Yao, Hot deformation behavior and dynamic recrystallization of GH690 nickel-based superalloy [J], J. Alloy. Compd. 847 (2020), https://doi.org/10.1016/j.jallcom.2020.156507 156507.
[20] X.D. Liu, J.K. Fan, K.D. Li, Y.L. Song, D.G. Liu, R.H. Yuan, J. Wang, B. Tang, H.C. Kou, J.S. Li, Serrated flow behavior and microstructure evolution of Inconel 625 superalloy during plane-strain compression with different strain rates [J], J. Alloy. Compd. 881 (2021), https://doi.org/10.1016/j.jallcom.2021.160648 160648.
[21] G. Tan, H.Z. Li, Y. Wang, S.C. Qiao, L. Yang, Z.Q. Huang, T.W. Cheng, Z.X. Zhao, Effect of Zener-Hollomon parameter on microstructure evolution of a HEXed PM nickel-based superalloy [J], J. Alloy. Compd. 874 (2021), https://doi.org/10.1016/j.jallcom.2021.159889 159889.
[22] H. Cheng, Y.C. Lin, D.G. He, Y.L. Qiu, J.C. Zhu, M.S. Chen, Influences of stress-aging on the precipitation behavior of δ phase (Ni_3Nb) in a nickel-based superalloy [J], Mater. Des. 197 (2021), https://doi.org/10.1016/j.matdes.2020.109256 109256.
[23] S.G. Protasova, G. Gottstein, D.A. Molodov, V.G. Sursaeva, L.S. Shvindlerman, Triple junction motion in aluminum tricrystals [J], Acta Mater. 49 (2001) 2519–2525, https://doi.org/10.1016/s1359-6454(01)00142-2.
[24] H. Miura, S. Andiarwanto, K. Sato, T. Sakai, Preferential dynamic nucleation at triple junction in copper tricrystal during high-temperature deformation [J], Mater. Trans. 43 (2002) 494–500, https://doi.org/10.2320/matertrans.43.494.
[25] S. Andiarwanto, H. Miura, T. Sakai. Dynamic recrystallization at triple junction during high-temperature deformation in copper tricrystal. D.N. Lee. Textures of Materials [M], 2002: 761–766, https://doi.org/10.4028/www.scientific.net/MSF.408-412.761.
[26] H.E. Sabzi, X.H. Li, C. Zhang, H. Fu, D. San Martín, P.E.J. Rivera-Díaz-del-Castillo. Deformation twinning-induced dynamic recrystallization during laser powder bed fusion [J]. Scripta Mater. 207 (2022) 114307, https://doi.org/10.1016/j.scriptamat.2021.114307.
[27] Z. Jia, Z.X. Gao, J.J. Ji, D.X. Liu, T.B. Guo, Y.T. Ding, Evolution of twin boundaries and contribution to dynamic recrystallization and grain growth of Inconel 625 [J], Adv. Eng. Mater. 21 (2019) 1900426, https://doi.org/10.1002/adem.201900426.
[28] H. Miura, T. Sakai, H. Hamaji, J.J. Jonas, Preferential nucleation of dynamic recrystallization at triple junctions [J], Scr. Mater. 50 (2004) 65–69, https://doi.org/10.1016/j.scriptamat.2003.09.035.
[29] G. Gottstein, L.S. Shvindlerman, A novel concept to determine the mobility of grain boundary quadruple junctions [J], Scr. Mater. 52 (2005) 863–866, https://doi.org/10.1016/j.scriptamat.2005.01.008.
[30] B.C. Xie, H. Yu, T. Sheng, Y.H. Xiong, Y.Q. Ning, M.W. Fu, DDRX and CDRX of an as-cast nickel-based superalloy during hot compression at γ′ sub-/super-solvus temperatures [J], J. Alloy. Compd. 803 (2019) 16–29, https://doi.org/10.1016/j.jallcom.2019.06.202.
[31] B.C. Xie, B.Y. Zhang, Y.Q. Ning, M.W. Fu, Mechanisms of DRX nucleation with grain boundary bulging and subgrain rotation during the hot working of nickel-based superalloys with columnar grains [J], J. Alloy. Compd. 786 (2019) 636–647, https://doi.org/10.1016/j.jallcom.2019.01.334.
[32] K. Zhang, B. Holmedal, T. Mánik, A. Saai, Assessment of advanced Taylor models, the Taylor factor and yield-surface exponent for FCC metals [J], Int. J. Plasticity. 114 (2019) 144–160, https://doi.org/10.1016/j.ijplas.2018.10.015.
[33] I.J. Moore, M.G. Burke, E.J. Palmiere, Modelling the nucleation, growth and coarsening kinetics of γ″ ($D0_{22}$) precipitates in the Ni-base Alloy 625 [J], Acta Mater. 119 (2016) 157–166, https://doi.org/10.1016/j.actamat.2016.08.027.
[34] P.J. Clemm, J.C. Fisher, The influence of grain boundaries on the nucleation of secondary phases [J], Acta Mater. 3 (1955) 70–73, https://doi.org/10.1016/0001-6160(55)90014-6.
[35] K. Huang, R.E. Logé, A review of dynamic recrystallization phenomena in metallic materials [J], Mater. Des. 111 (2016) 548–574, https://doi.org/10.1016/j.matdes.2016.09.012.
[36] B.C. Xie, B.Y. Zhang, H. Yu, H. Yang, Q. Liu, Y.Q. Ning, Microstructure evolution and underlying mechanisms during the hot deformation of 718Plus superalloy [J], Mater. Sci. Eng. A 784 (2020), https://doi.org/10.1016/j.msea.2020.139334 139334.
[37] J.C. Stinville, E.R. Yao, P.G. Callahan, J. Shin, F. Wang, M.P. Echlin, T.M. Pollock, D.S. Gianola, Dislocation dynamics in a nickel-based superalloy via in-situ transmission scanning electron microscopy [J], Acta Mater. 168 (2019) 152–166, https://doi.org/10.1016/j.actamat.2018.12.061.
[38] G. Liu, J. Salvat Cantó, S. Winwood, K. Rhodes, S. Birosca, The effects of microstructure and microtexture generated during solidification on deformation micromechanism in IN713C nickel-based superalloy [J], Acta Mater. 148 (2018) 391–406, https://doi.org/10.1016/j.actamat.2018.01.062.